Effect of a Charge Relay on the Vibrational Frequencies of Carbonmonoxy Iron Porphine Adducts: The Coupling of Changes in Axial Ligand Bond Strength and Porphine Core Size

Stefan Franzen

Contribution from the Department of Chemistry, North Carolina State University, Raleigh, North Carolina 27695

Received April 9, 2001

Abstract: The effect of a charge relay involving Asp-His-Fe in peroxidase enzymes is explored using density functional theory (DFT) calculations of vibrational spectra and potential energy surfaces of carbonmonoxy model systems. The series of models consists of a carbonmonoxy iron porphine molecule with a trans imidazole ligand hydrogen-bonded to six different partners at the Nδ position. Calculations on the oxy system and on models of the Asp-His-Ser catalytic triad of serine proteases were also performed to obtain an understanding of how the redistribution of charge in these systems may contribute to enzymatic function. The goal of the study is to relate the experimental frequencies in resonance Raman and Fourier transform infrared studies to bonding that is important for the function of heme enzymes. Calculations of both axial and in-plane modes exhibit trends that agree with experimental data. Comparisons of the charge distribution on the different models show that polarization of iron carbonomonoxy bonds consistent with the mechanism for peroxidase function leads to a frequency reduction in the C−O stretching mode ν_{CO}. The combination of axial trans σ-bonding and π-bonding effects that include expansion of the porphine core result in little change in the Fe−C stretching frequency ν_{Fe-CO} in the series of molecules studied with different Nδ−H hydrogen bonding. A particular role for the core size is discussed that demonstrates the applicability of trends observed in vibrational spectroscopy of hemes to the charge relay mechanism and other axial ligation effects. The bonding interactions described account for the increase in electron density on bound diatomic ligands, which is required for peroxidase function.

Introduction

Charge relay mechanisms are key to the modulation of reactivity at the heme iron in heme proteins.[1–3] A charge relay consists of a hydrogen bonding network that tunes the basicity of an axial ligand to the heme iron to support oxidation states greater than Fe(III).[2,4] The Fe(IV) iron oxidation state is important in peroxidases, oxidases, monooxygenases, catalases, and other heme enzymes where homo- or heterolytic cleavage of bound oxygen or peroxide occurs. The Fe(IV) oxo intermediates known as compound **I** and compound **II** are stabilized by negative charge density on imidazole, cysteinate, or tyrosinate. The protein electrostatic environment stabilizes anionic cysteinate ligation of the heme in the cytochrome P450 superfamily.[5] Specific hydrogen bonding interactions stabilize tyrosinate in catalase.[3] In peroxidases, where imidazole is polarized by the electrostatic interactions with aspartate or other protein residues, the fine-tuning of reactivity by changes in electrostatic environment is a major determinant of the electron density on the bound oxy or peroxy species. A charge relay involving hydrogen bonding has been suggested in cytochrome *c* peroxidase, sulfite reductase, and CooA.[2,4,6] The specific mechanism

for control of histidine reactivity and stability is apparent in the hydrogen bonding to the Nδ−H hydrogen of histidine in globins, oxidases, peroxidases, and a large number of other heme enzymes.[7] Figure 1 shows a proposed charge relay derived from studies of peroxidases where aspartate (modeled as acetate) forms a strong hydrogen bond to the Nδ−H position of histidine (modeled as imidazole) to form an Asp-His-Fe charge relay. Distal effects are also important, and these enzymes typically have appropriate histidine or arginine side chains capable of controlling the protonation state of bound intermediates;[8–13] however, distal effects are not included in this study. The present study addresses the proximal effect of such a charge relay on electronic structure by connecting vibrational spectroscopic data from studies of the carbonmonoxy adducts to a bonding picture relevant for the proximal charge relay in histidine-ligated heme enzymes.

Carbon monoxide has been a common diatomic ligand for studies of heme protein electrostatic effects and dynamics. CO

(1) Spiro, T. G.; Smulevich, G.; Su, C. *Biochemistry* **1990**, *29*, 4497–4508.

(2) Goodin, D. B.; McRee, D. E. *Biochemistry* **1993**, *32*, 3313–3324.

(3) Putnam, C. D.; Arvai, A. S.; Bourne, Y.; Tainer, J. A. *J. Mol. Biol.* **2000**, *296*, 295–309.

(4) Vogel, K. M.; Spiro, T. G.; Shelver, D.; Thorsteinsson, M. V.; Roberts, G. P. *Biochemistry* **1999**, *38*, 2679–2687.

(5) Poulos, T. L.; Raag, R. *FASEB J.* **1992**, *6*, 674–679.

(6) Crane, B. R.; Siegel, L. M.; Getzoff, E. D. *Biochemistry* **1997**, *36*, 12101–12119.

(7) Decatur, S. M.; Belcher, K. L.; Rickert, P. K.; Franzen, S.; Boxer, S. G. *Biochemistry* **1999**, *38*, 11086–11092.

(8) Das, T. K.; Friedman, J. M.; Kloek, A. P.; Goldberg, D. E.; Rousseau, D. L. *Biochemistry* **2000**, *39*, 837–842.

(9) Balasubramanian, S.; Lambright, D. G.; Boxer, S. G. *Proc. Natl. Acad. Sci. U.S.A.* **1993**, *90*, 4718–4722.

(10) Kim, S.; Deinum, G.; Gardner, M. T.; Marletta, M. A.; Babcock, G. T. *J. Am. Chem. Soc.* **1996**, *118*, 8769–8770.

(11) Kushkeley, B.; Stavrov, S. *Biophys. J.* **1996**, *70*, 1214–1229.

(12) Cameron, A. D.; Smerdon, S. J.; Wilkinson, A. J.; Habash, J.; Helliwell, J. R.; Li, T. S.; Olson, J. S. *Biochemistry* **1993**, *32*, 13061–13070.

(13) Ling, J. H.; Li, T. S.; Olson, J. S.; Bocian, D. F. *Biochim. Biophys. Acta: Bioenergetics* **1994**, *1188*, 417–421.
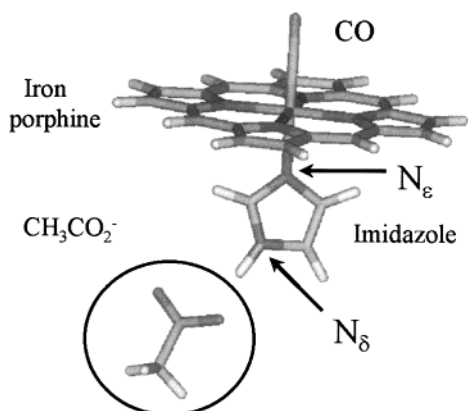
Figure 1. Stick representation of the imidazole carbonmonoxy iron porphine adduct with acetate hydrogen bonded to the Nδ–H position of imidazole. The circle identifies the substitution site in the model calculations. The charge relay is modeled by replacing acetate by a range of hydrogen bond partners given in Table 1. The model structure represents the Asp-His-Fe catalytic triad found in peroxidase enzymes.

is inert, and yet Fe–CO and C–O stretching bands observed in resonance Raman and infrared (IR) spectra[1,11,14–21] serve as sensitive probes of the electrostatic environment in a range of heme proteins including peroxidases, oxidases, monooxygenases, prostaglandin synthase, and globins.[19,22–26] Calculated substituent effects can be divided into trans-effects (proximal), cis-effects (equatorial), and distal effects (see Figure 1). Recently, semiempirical calculations have been applied to the study of proximal/distal side effects using a point charge model,[11] and density Functional theory (DFT) calculations of model meso-substituted porphines have been used to model equatorial substituent effects.[27] A number of studies have also addressed various aspects of hydrogen bond effects on the distal side.[28–32] The calculated effects agree with the experimentally determined inverse correlation of Fe–CO and C–O stretching

mode frequencies known as π-back-bonding.[1] A strengthening of the Fe–C bond due to an increase in dπ electron density on the iron decreases the strength of the C–O bond by putting more electron density into the π* orbital of bound CO. The role of the trans-effect is of great interest because of its functional relevance. Moreover, orbital symmetry suggests that strong hydrogen bonding to Nδ–H results in strong σ-bonding of Nϵ to the heme iron in addition to the π-bonding interactions that are evident in the experimental data. In fact, the strong σ-donor character of mercaptide ligands has been shown by both experiment and calculation to lower the frequency of the Fe–CO and C–O stretches in parallel.[1,27] Polarization of imidazole should also affect the σ-donor character of the Nϵ lone pair, a key step in the charge relay mechanism responsible for increasing electron density on heme-bound diatomic ligands and peroxide. The present density functional theory (DFT) study of the effect charge relay on the C–O potential surface addresses the nature of the trans-effect due to hydrogen bond interactions with Nδ–H of the proximal imidazole by comparison with experimental data on the vibrational frequencies of both in-plane and axial ligand modes.

Our approach to modeling the spectra is to use DFT to calculate vibrational spectra and potential energy surfaces for a series of trans imidazoles and imidazolates in the iron–porphine–CO adduct shown in Figure 1. Figure 1 shows aspartate hydrogen bonded to the imidazole at the Nδ–H position. A series of hydrogen bond donors given in Table 1 were compared in order to systematically modulate the charge density on the iron. The genesis of this model is the well-studied hydrogen-bonding of Asp235 to His175 in cytochrome *c* peroxidase.[2] This hydrogen-bond pattern presents a catalytic triad of Asp-His-Fe in peroxidases analogous to the Asp-His-Ser of serine proteases shown in Figure 2. A similar motif appears in a number of enzymes, including cysteine proteases and even selenocysteine proteases and peroxidases.[33,34] In the hydrolytic enzymes, the role of Asp in the triad is to increase the basicity of the imidazole ring of histidine. The σ-donor strength of the histidine in turn polarizes the nucleophilic ligand (serine, cysteine, or selenocysteine) by increased hydrogen bond strength.[33,34] Our study investigates the role of both σ-bonding and π-bonding induced by a change in electron density on the imidazole ligand trans to bound CO. These effects are compared to a model for charge relay in serine proteases, the catalytic triad Asp-His-Ser shown in Figure 2. One significant difference between the proteases and peroxidases is the presence of the heme (here modeled by porphine). The effect of altered electron density at the heme iron is complicated by equatorial (cis) effects on the porphine ring due to changes in the iron core size. This effect is key to the effects of various proximal ligands or changes in the basicity of the imidazole of globins and peroxidases. The goal of this theoretical study is to understand the information presented by the correlation of vibrational frequencies of the $\nu_{Fe–CO}$ and ν_{CO} stretching modes and the core size marker modes that consist of non-totally symmetric modes ν_{10} and ν_{11} as well as totally symmetric modes ν_2 and ν_3. We consider the functional relevance of σ-bonding as it affects both trans and cis π-bonding by expansion of the iron core.

The analogy between Asp-His-Ser and Asp-His-Fe is examined in light of the differences in π-bonding in the two systems. The extent of hydrogen bonding or deprotonation at Nδ on the basicity at Nϵ in the Asp-His-Ser system shown in Figure 2 determines the relative energy of the Nϵ lone pair that is

(14) Ramsden, J.; Spiro, T. G. *Biochemistry* **1989**, *28*, 3125–3128.

(15) Ray, G. B.; Li, X.-Y.; Ibers, J. A.; Sessler, J. L.; Spiro, T. G. *J. Am. Chem. Soc.* **1994**, *116*, 162–176.

(16) Lim, M.; Jackson, T. A.; Anfinrud, P. A. *Science* **1995**, *269*, 962–965.

(17) Laberge, M.; Vanderkooi, J. M.; Sharp, K. A. *J. Phys. Chem. B* **1996**, *100*, 10793–10801.

(18) Anderton, C. L.; Hester, R. E.; Moore, J. N. *Biochim. Biophys. Acta* **1997**, *1338*, 107–120.

(19) Phillips, J., G. N.; Teodoro, M. L.; Li, T.; Smith, B.; Olson, J. S. *J. Phys. Chem. B* **1999**, *103*, 8817–8829.

(20) Kaposi, A. J.; Fidy, J.; Manas, E. S.; Vanderkooi, J. M.; Wright, W. W. *Biochim. Biophys. Acta* **1999**, *1435*, 41–50.

(21) Decatur, S. M.; Boxer, S. G. *Biochem. Biophys. Res. Commun.* **1995**, *212*, 159–164.

(22) Evangelista-Kirkup, R.; Smulevich, G.; English, A.; Spiro, T. G. *Biochemistry* **1986**, *25*, 4420–4425.

(23) Park, K. D.; Guo, K.; Adebodun, F.; Chiu, M. L.; Sligar, S. G.; Oldfield, E. *Biochemistry* **1991**, *30*, 2333–2347.

(24) Uno, T.; Nishimura, Y.; Tsuboi, M.; Makino, R.; T, I.; Iashimura, Y. *J. Biol. Chem.* **1987**, *262*, 4549–4556.

(25) Tsubaki, M.; Srivastava, R. B.; Yu, N.-T. *Biochemistry* **1982**, *21*, 1132–1140.

(26) Lou, B. S.; Snyder, J. K.; Marshall, P.; Wang, J. S.; Wu, G.; Kulmacz, R. J.; Tsai, A. L.; Wang, J. L. *Biochemistry* **2000**, *39*, 12424–12434.

(27) Vogel, K. M.; Kozlowski, P. M.; Zgierski, M. Z.; Spiro, T. G. *Inorg. Chim. Acta* **2000**, *297*, 11–17.

(28) Groot, M. J. d.; Havenith, R. W. A.; Vinkers, H. M.; Zwaans, R.; Vermeulen, N. P. E.; Lenthe, J. H. v. *J. Comput.-Aided. Mol. Des.* **1998**, *12*, 183–193.

(29) Wirstam, M.; Blomberg, M. R. A.; Siegbahn, P. E. M. *J. Am. Chem. Soc.* **1999**, *121*, 10178–10185.

(30) Loew, G.; Dupuis, M. *J. Am. Chem. Soc.* **1996**, *118*, 10584–10587.

(31) Kuramochi, H.; Noodleman, L.; Case, D. A. *J. Am. Chem. Soc.* **1997**, *119*, 11442–11451.

(32) Nishida, Y. *Inorg. Chem. Commun.* **2000**, *3*, 310–312.

(33) Buhling, F.; Fengler, A.; Brandt, W.; Welte, T.; Ansorge, S.; Nagler, D. K. *Cell. Peptidases Immune Funct. Dis.* **2000**, *477*, 241–254.

(34) Arthur, J. R. *Cell. Mol. Life Sci.* **2000**, *57*, 1825–1835.

Table 1. Ligands and Hydrogen Bond Partners Studied by Density Functional Theory

acronym	proximal ligand (dihedral angle, deg)	Nδ−H hydrogen bond species	H-bond distance	H-bond angle	heme deformation[a]
IM	imidazole (3)	NA	NA	none	none
IM45	imidazole (44)	NA	NA	none	none
IMH2	imidazole (1)	H_2O	Nδ−HO (1.97 Å)	Nδ−H−O−H (119.5°)	none
IMNMA	imidazole (32)	*N*-methylacetamide	Nδ−HO (1.79 Å)	Nδ−H−O= (158.25°)	ruffling (B_{1u})
IMACET	imidazole (42)	acetate	Nδ−HO (1.50 Å)	Nδ−H−O−C (108.67°)	waving (E_g)
IMA	imidazolate (1)	NA	NA	NA	ruffling (B_{1u})
IMAH2	imidazolate (6)	H_2O	Nδ−HO (1.82 Å)	Nδ−H (179.62°)	ruffling (B_{1u})
H2O	H_2O	NA	NA	NA	doming (A_{2u})
5CO	NA	NA	NA	NA	doming (A_{2u})

[a] Following the classification of Shelnutt.[55]
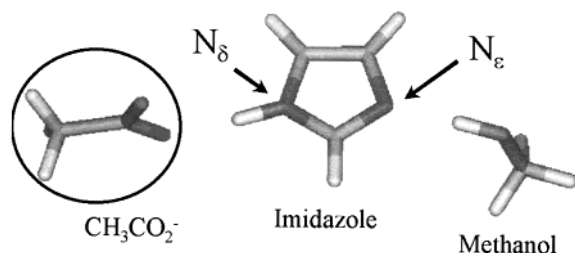
Figure 2. Stick model of the catalytic triad of serine proteases with acetate hydrogen bonded to the Nδ−H position of imidazole. The circle identifies the substitution site in the model calculations. The charge relay was modeled for the same set of hydrogen bond partners as the iron porphine system. The model structure represents the Asp-His-Ser molecular charge relay hypothesized to account for the reactivity of serine proteases.

involved in a hydrogen bond with the serine hydroxyl group. For serine proteases, this hydrogen bonding interaction results in greater electron density on the catalytic serine nucleophile. Despite these differences, strong similarities emerge from the DFT calculations. One of the major similarities of the two systems that will emerge from our study is that the charge density on the oxygen atom of methanol (Figure 2), the terminal oxygen of bound carbon monoxide, or bound dioxygen (Figure 1) increases as a result of Nδ−H hydrogen bonding. Moreover, the serine O−H, porphine Fe−CO bond, and C−O bonds are all three weakened by increasing polarization of the imidazole in the relay. This polarization is transmitted through both σ- and π-effects, and our hypothesis is that the π-effect is required to achieve the type of reactivity found in peroxidases. The charge density on dioxygen increases, and the O−O bond becomes more dipolar. The net effect is to increase the charge on the terminal oxygen (i.e. $Fe^{\delta+}$−O−$O^{\delta-}$). The partial negative charge facilitates protonation of the terminal oxygen, which leads to the O−O scission step and compound **I**, PFe^{III}−O−O−H + H^+ → P^+Fe^{IV}=O + H_2O. The increased π-density is required for polarization because trans σ-bonding alone would repel the peroxy ligand, strengthen the O−O bond, and reduce electron density on the terminal oxygen. Moreover, increased π-bonding provides some stabilization of the oxo ferryl species (P^+Fe^{IV}=O) required for homolytic cleavage. It is noteworthy that hydrogen bonding of the proximal ligand, an inherently σ-bonding interaction, can effect changes in π-bonding through the effect on the iron core size of the porphyrin ring.

Our study compares well with the body of prior experimental[35−38] and theoretical work (see Supporting Information).[29,31,39−44] The calculations presented show experimental

correlations for axial Fe−CO, C−O, core size marker, and electron density marker modes that demonstrate the effect of axial ligands on the heme active site electronic structure. The experimental trends in core size marker modes are also observed in the DFT calculated frequencies. The dependence of the electron density marker mode (ν_4) on the coordination sphere is observed. The present study quantifies the increase in charge density on the terminal oxygen that leads to the weakened O−O bond necessary for peroxidase function. Although peroxide binding is functionally important, it is difficult to observe peroxy adducts experimentally and even dioxygen has not been extensively studied due to autoxidation problems and the low resonance Raman cross-section. Therefore, we focus on the large body of experimental data available on CO adducts. The procedure has application to the wide range of heme enzymes with various charge relay systems that provide control over heme iron reactivity throughout the family of heme enzymes. The present study further establishes the role of CO as a probe since it explains the trends in the ν_{CO} stretching frequencies in terms of their charge distribution and changes in proximal ligation. This study suggests the need for further work to clarify the complementary role of distal side interactions with bound CO.

Methods

The optimized ground-state geometries were obtained using both the generalized gradient approximation (GGA) of Perdew and Wang[45] and the BLYP functional[46,47] as implemented in DMol3 (Molecular Simulations Inc.).[48,49] All calculations were carried out on the SGI/ Cray Origin 2000 and IBM SP supercomputers at the North Carolina Supercomputer Center (NCSC). A numerically tabulated basis set of double-ζ plus quality was employed as described in the Supporting Information. The geometry optimizations were carried out until the energy difference was less than 10^{-6} a.u. on subsequent iterations. Following geometry optimization the Hessian matrix was constructed by finite difference. Calculations on the M1 model were carried out using Gaussian98 at the NCSC.[50] The M1 model consists of the imidazole−iron−CO moieties in Figure 1 with the porphine ring replaced by four amidinato ($-NH_2^-$) groups (see Supporting Informa-

(35) Choi, S.; Spiro, T. G.; Langry, K. C.; Smith, K. M.; Budd, L. D.; LaMar, G. N. *J. Am. Chem. Soc.* **1982**, *104*, 4345-.

(36) Feitelson, J.; Spiro, T. G. *Inorg. Chem.* **1986**, *25*, 861−865.

(37) Hu, S.; Smith, K. M.; Spiro, T. G. *J. Am. Chem. Soc.* **1996**, *118*, 12638−12646.

(38) Li, X. Y.; Czernuszewicz, R. S.; Kincaid, J. R.; Su, Y. O.; Spiro, T. G. *J. Phys. Chem.* **1990**, *94*, 31−47.

(39) Ghosh, A.; Bocian, D. F. *J. Phys. Chem.* **1996**, *100*, 6363−6367.

(40) Rovira, C.; Kunc, K.; Hutter, J.; Ballone, P.; Parrinello, M. *J. Phys. Chem. A* **1997**, *101*, 8914−8925.

(41) Rovira, C.; Parrinello, M. *Chem.− Eur. J.* **1999**, *5*, 250−262.

(42) Rovira, C.; Parrinello, M. *Int. J. Quantum Chem.* **1998**, *70*, 387−394.

(43) Vogel, K. M.; Kozlowski, P. M.; Zgierski, M. Z.; Spiro, T. G. *J. Am. Chem. Soc.* **1999**, *121*, 9915−9921.

(44) Harvey, J. N. *J. Am. Chem. Soc.* **2000**, *122*, 12401−12402.

(45) Perdew, J. P.; Chevary, J. A.; Vosko, S. H.; Jackson, K. A.; Pederson, M. R.; Singh, D. J.; Fiolhais, C. *Phys. Rev. B* **1992**, *46*, 6671−6687.

(46) Becke, A. D. *J. Chem. Phys.* **1997**, *107*, 8554−8560.

(47) Lee, C. L.; Yang, W.; Parr, R. G. *Phys. Rev. B* **1988**, *37*, 785−789.

(48) Delley, B. *J. Chem. Phys.* **1990**, *92*, 508−517.

(49) Delley, B. *J. Chem. Phys.* **2000**, *113*, 7756−7764.

Table 2. Selected Bond Lengths Obtained from DFT Geometry Optimized Structures of Iron−Porphine−CO Models (GGA-PW92/BLYP)

structure	Fe−C GGA	Fe−C BLYP	C−O GGA	C−O BLYP	Fe−Np GGA	Fe−Np BLYP	Fe−Ne GGA	Fe−Nε BLYP
IM	1.786	1.813	1.157	1.159	2.020	2.042	2.074	2.138
IMA	1.800	1.828	1.163	1.165	2.023	2.046	2.026	2.071
IMH2O	1.788	1.814	1.157	1.159	2.020	2.043	2.071	2.129
IMAH2O	1.804	1.824	1.161	1.164	2.022	2.046	2.049	2.077
IMNMA	1.790	1.819	1.158	1.160	2.021	2.045	2.053	2.096
IMACET	1.792	1.820	1.162	1.163	2.022	2.044	2.036	2.088
IM45	1.789	1.814	1.157	1.159	2.020	2.041	2.056	2.118
H2O	1.770	1.792	1.157	1.160	2.023	2.038	2.156	2.216
5CO	1.745	1.765	1.160	1.162	2.011	2.027	NA	NA

tion). Comparative geometry optimizations on the M1 model were carried out using Hartree−Fock (HF),[51] second-order Møller−Plesset peturbation theory (MP2)[52,53] and the BLYP functional[46,47] with a 6-31G** basis set. AVS (Advanced Visual System) and insightII (Molecular Simulations) programs were used for visualization of the results. Conversion from Cartesian to internal coordinates and decomposition of the potential energy distribution (PED) was carried out using the program FCART.[54]

Results and Discussion

Geometry Optimized Structures. There are significant differences that emerge as the hydrogen bonding of the axial imidazole ligand is altered: the axial imidazole can rotate from the initial position; the heme geometry can distort from a planar starting geometry; the bond lengths of the axial ligands can be altered. Table 1 gives the dihedral angles for the imidazole ligands, porphine geometry changes, and the hydrogen bonding geometry of Nδ−H of the various hydrogen-bond-forming moieties (H_2O, CH_3COO^-, $CH_3CONHCH_3$).

The Np−Fe−Nε−Cδ dihedral angles for the imidazole were initially at 0° prior to geometry optimization (except in the IM45 structure where the dihedral angle τ was set to 45° at the outset of the geometry optimization). [The following abbreviations have been used for atoms in the structure shown in Figure 1: Np, pyrrole nitrogen of the porphine ring; Nε, the nitrogen of imidazole that is bonded to Fe; Nδ, the nitrogen of imidazole the is protonated; Cδ, the carbon of imidazole bonded to Nε and Nδ.] Since the imidazole ligands were not constrained in the calculations performed here, there are a variety of dihedral angles τ in the different species as seen in column 2 of Table 1. The imidazole ligand to iron shows modest rotation in the IM, IMA, IMH2O, and IMAH2O models (column 2, Table 1). However, when a larger, more polarizable group hydrogen bonds to Nδ−H the dihedral angle increases (column 2, Table 1). The dihedral angle of axial neutral imidazole was studied by comparison of an imidazole with a starting geometry at $\tau = 0°$ (IM) and one at $\tau = 45°$ (IM45). The effect of a rotation of the proximal ligand was found to be modest. The shorter Fe−Nε bond length for $\tau = 45°$ is consistent with the intuition that the

Table 3. Correlation Table of Distances in the Porphine Iron Coordination Sphere and the Bound Carbon Monoxide

correlation	GGA intercept, slope (R)	BLYP intercept, slope (R)
Fe−C vs Fe−Nε	2.29, −0.24 (0.67)	2.24, −0.20 (0.95)
C−O vs Fe−Nε	1.40, −0.12 (0.86)	1.35, −0.09 (0.89)
Fe−Np vs Fe−Nε	2.11, −0.04 (0.74)	2.15, −0.05 (0.88)
Fe−Np vs Fe−C	1.76, 0.15 (0.93)	1.63, 0.23 (0.85)
Fe−Np vs C−O	1.62, 0.35 (0.84)	1.63, 0.35 (0.65)
C−O vs Fe−C	0.58, 0.32 (0.86)	0.34, 0.45 (0.93)

axial ligand will have less steric hindrance with the pyrrole nitrogens if the imidazole is not aligned along the Np−Fe−Np bonds. The effect on in-plane vibrational modes is slight, but there is significant effect on $\nu_{Fe−CO}$ and ν_{CO} (see below).

Changes in porphine structure can be decomposed into changes in in-plane structural coordinates and changes in out-of-plane structural coordinates. Table 1 shows the out-of-plane structural changes. Table 1 indicates that the IMA, IMAH2O, and IMNMA structures are deformed along a B_{1u} normal coordinate (ruffling). The IMACET structure is distorted along an E_u normal coordinate (i.e. waving). The distortions from planar geometry in D_{4h} have been categorized by Shelnutt.[55,56] The in-plane structural changes consist mainly of core size expansion, which is described here as an increase in the Fe−Np bond length. In the following the average Fe−Np bond length is considered as an indicator of the porphine core size.

The geometries obtained from the two DFT functionals are very similar. The Fe−Nε bonds are ≈2.5% longer in the BLYP calculation (see Table 2). The Fe−C and Fe−Np bond lengths are ≈1% longer, and the C−O bonds are ≈0.2% longer in the BLYP calculation than in the GGA-PW92 calculation.

The correlations between the various bond lengths given in Table 3 show a distinct pattern where the Fe−C, C−O, and Fe−Np bond lengths are inversely proportional to Fe−Nε and directly proportional to each other. Table 3 shows correlations based on a fit to a line. The parameters for the fit, including the correlation coefficient R, are given in Table 3 as well. The negative slope for lines where d(Fe−C), d(C−O), and d(Fe−Np) are plotted as a function of d(Fe−Nε) shows an inverse proportionality between these bond lengths throughout the series studied here. Increasing ligation strength leads to a shorter Fe−Nε bond and an expansion of the core size and an increase in the iron−carbon distance. The shortening of the Fe−Nε bond also leads to a lengthening of the C−O bond. This observation is of central importance in the description that follows. These relationships imply that the bond lengths d(Fe−C) and d(C−O) are directly proportional to d(Fe−Np) and to each other for the same set of structures. The porphine core is found to be

(50) Frisch, M. J.; G. W. T.; Schlegel, H. B.; Scuseria, G. E.; Robb, M. A.; J. R. C.; Zakrzewski, V. G.; Montgomery, J. A., Jr.; Stratmann, R. E.; J. C. B.; Dapprich, S.; Millam, J. M.; Daniels, A. D.; K. N. K.; Strain, M. C.; Farkas, O.; Tomasi, J.; Barone, V.; M. C.; Cammi, R.; Mennucci, B.; Pomelli, C.; Adamo, C.; Clifford, S.; J. O.; Petersson, G. A.; Ayala, P. Y.; Cui, Q.; Morokuma, K.; D. K. M.; Rabuck, A. D.; Raghavachari, K.; Foresman, J. B.; J. C.; Ortiz, J. V.; Stefanov, B. B.; Liu, G.; Liashenko, A.; P. P.; Komaromi, I.; Gomperts, R.; Martin, R. L.; Fox, D. J.; T. K.; Al-Laham, M. A.; Peng, C. Y.; Nanayakkara, A.; Gonzalez, C.; M. C.; Gill, P. M. W.; Johnson, B.; Chen, W.; Wong, M. W.; Andres, J. L.; Gonzalez, C.; Head-Gordon, M.; Replogle, E. S.; Pople, J. A. *Gaussian98*; Gaussian, Inc.: Pittsburgh, PA, 1998.

(51) Roothan, C. C. J. *Rev. Mod. Phys.* **1951**, *23*, 69−76.

(52) Saebo, S.; Almlof, J. *Chem. Phys. Lett.* **1989**, *154*, 83−89.

(53) Frisch, M. J.; Head-Gordon, M.; Pople, J. A. *Chem. Phys. Lett.* **1990**, *166*, 275−280.

(54) Collier, W. B. *J. Chem. Phys.* **1988**, *88*, 7295−7305.

(55) Jentzen, W.; Ma, J. G.; Shelnutt, J. A. *Biophys. J.* **1998**, *74*, 753−763.

(56) Howes, B. D.; Schiodt, C. B.; Welinder, K. G.; Marzocchi, M. P.; Ma, J. G.; Zhang, J.; Shelnutt, J. A.; Smulevich, G. *Biophys. J.* **1999**, *77*, 478−492.

the largest for anionic ligands and somewhat smaller for the hydrogen-bonded species IMNMA and IMACET. [The designation anionic species refers to the models that have a −1 overall charge. These are IMA, IMAH2O, and IMACET. IMA is deprotonated, and the imidazole is imidazolate anion. The IMAH2O model was geometry optimized starting with neutral imidazole hydrogen bonded to hydroxide anion. At the end of the geometry optimization the imidazole was deprotonated, so the structure is imidazolate hydrogen bonded to H_2O. The IMACET structure is imidazole hydrogen bonded to acetate both at the beginning and at the end of geometry optimization.] The core is the smallest for neutral imidazole (IM) and imidazole with $N\delta$−H hydrogen-bonded to H_2O. The core size expansion plays an important role in the charge relay by converting σ-bonding interactions that lead to the $d(Fe-N\epsilon) - d(Fe-C)$ correlation into the π-bonding interactions that lead to the $d(Fe-N\epsilon) - d(C-O)$ correlation.

The role of steric repulsion on the $Fe-N\epsilon$ bond length is seen in the comparison of IM and IM45 models (see Table 1). The $Fe-N\epsilon$ bond length shortens significantly for the IM45 geometry. In the GGA calculation the core size does not change. However, in the BLYP calculation of IM45 $d(Fe-Np)$ is the smallest of any nitrogenous adduct in the series. The calculated trend indicates that the core size tends to expand as the ligand donor strength increases and not just due to shortening of the $Fe-N\epsilon$ bond, but also due to charge displacement onto the iron. In the following we consider how these structural trends depend on the electron density of the imidazole $N\epsilon$ position acting through a charge relay. The structural considerations indicate that one should consider both axial and equatorial bonding effects evident in vibrational spectra and calculated charge density.

The correlation of the $Fe-C$ and $C-O$ bond lengths is crucial to understanding the origin of charge relay effects and the relationship they have to observables such as vibrational frequencies. The bond lengths of the species given in Table 2 do not show a π-back-bonding correlation as the axial ligation strength is altered. Rather than an inverse relationship between $d(Fe-C)$ and $d(C-O)$ bond lengths expected based on the experimental frequency correlation we find that $d(Fe-C)$ and $d(C-O)$ change in parallel (see Table 3). For example, the $Fe-C$ is 0.7% longer on average for the anionic species (IMA, IMAH2O, IMACET) compared to neutral imidazole (IM). The effect on the $C-O$ bond length is somewhat smaller (0.4% longer on average) but still in parallel with the change in the $Fe-C$ bond length. By contrast, an inverse relationship between $d(Fe-C)$ and $d(C-O)$ is maintained when one compares imidazole (IM), the H_2O axial ligand (H2O in Table 1), and the five-coordinate iron porphine (5CO). It is clear from comparison from these considerations that there are competing effects. The nature of competing σ-bonding and π-bonding effects is considered further below in studies of the charge density shifts and change in axial bonding for the atoms $N\delta-N\epsilon-Fe-C-O$ due to the charge relay.

Vibrational Spectra. In-Plane Porphine Vibrations. The calculated in-plane frequencies shown in Figure 3 follow the experimental trends in the well-studied core size marker modes ν_2, ν_3, ν_{10}, and ν_{11} and the electron density marker, ν_4. The in-plane modes are denoted by their symmetry as Franck−Condon active A_{1g} modes or vibronically active B_{1g}, A_{2g}, and B_{2g} modes. The non-totally symmetric modes are observed in vibronic progression of the absorption spectrum or in the resonance Raman spectrum due to Herzberg−Teller interstate and Jahn−Teller intrastate coupling.[57] The frequencies of Raman active porphine in-plane vibrational modes given in Table 4 are in reasonable agreement with experimental data as well as
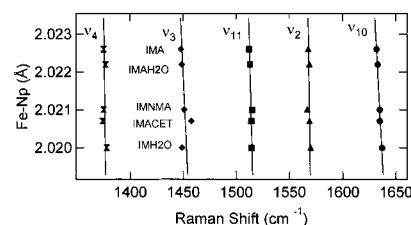

Figure 3. Plot of the core size marker modes and electron density marker mode for six-coordinate ferrous iron porphine model structures. The lines through data were obtained by fitting the data to eq 1 in ref 59. Fit parameters are given in the text.

other DFT treatments of the nickel porphine and iron porphine rings. [The frequencies included in Table 4 are those that have eigenvectors clearly indicative of modes of the gerade irreducible representations of D_{4h}. These modes include most of the commonly observed modes in Raman spectra of metalloporphyrins.] Nickel porphine has been shown to be a useful model for studies of hemes[38,58] and is used here to indicate the validity of the in-plane calculation. For example, the frequencies of the totally symmetric modes ν_2, ν_3, and ν_4 observed at 1574, 1459, and 1376 cm^{-1} in nickel porphine agree well with the calculated values for IM given in column 3 of Table 4 of 1563, 1449, and 1378 cm^{-1}, respectively.[38] A comparison of the calculated imidazole iron porphine CO adduct (IM) with 21 observed nickel porphine frequencies is given in Table 4 (compare columns 2 and 3). The average deviation for the observed in-plane modes is 1.3%. The in-plane BLYP frequencies are consistently 10− 20 cm^{-1} lower than GGA frequencies and show a somewhat poorer correlation with the NiP data. However, if these 21 modes are scaled, then a reasonable agreement is obtained. The origin of the lower frequencies is attributable to the larger core size found in the equilibrium geometry using the BLYP function. The average $Fe-Np$ distance is ≈2.04 Å for the BLYP functional and ≈2.02 Å for the GGA-PW92 functional. The frequencies can also be qualitatively compared to those of heme and heme models keeping in mind that the β-positions of the porphyrin ring have no substituents in the porphine model calculations (see Supporting Information).

The porphine core size increases as the axial ligand basicity increases. Figure 3 shows the frequency dependence of modes ν_2, ν_3, ν_4, ν_{10}, and ν_{11} on the average $Fe-Np$ distance for a series of six-coordinate model molecules studied using the Perdew−Wang GGA density functional. In the iron−porphine models considered here the core size expands most for imidazolate (IMA) and decreases in the series IMAH2O > IMNMA > IMACET > IMH2O. The ≈10 cm^{-1} vibrational frequency shifts in modes ν_2, ν_3, ν_{10}, and ν_{11} are consistent with experimentally observed core size effects.[59−61][The correlation of core size with frequency was fitted to the linear model function used previously in a number of reports.[59,61] The relation used was $\nu = K(A - d)$ cm^{-1}, where d is the average $Fe-Np$ distance and the parameters $K(cm^{-1}/Å)$ and A (Å) have the values 1789 and 2.93 for ν_{10}, 819 and 3.86 for ν_{11}, 431 and 5.66 for ν_2, and 1573 and 2.94 for ν_3. Although the trends are correct, the calculated dependence is a factor of 2−3 larger than the experimental correlation reported for ferric hemes.] The shift of the electron density marker band of ≈3 cm^{-1} is significantly

(57) Shelnutt, J. A. *J. Chem. Phys.* **1981**, *74*, 6644−6657.

(58) Rush, I., T. S.; Kozlowski, P. M.; Piffat, C. A.; Kumble, R.; Zgierski, M. Z.; Spiro, T. G. *J. Phys. Chem. B* **2000**, *104*, 5020−5034.

(59) Callahan, P. M.; Babcock, G. T. *Biochemistry* **1981**, *20*, 952−958.

(60) Friedman, J. M.; Rousseau, D. L.; Ondrias, M. R. *Annu. Rev. Phys. Chem.* **1982**, *33*, 471−491.

(61) Parthasarathi, N.; Hansen, C.; Yamaguchi, S.; Spiro, T. G. *J. Am. Chem. Soc.* **1987**, *109*, 3865−3871.

Table 4. Comparison of Selected In-Plane Vibrational Modes of A_{1g}, A_{2g}, B_{1g}, and B_{2g} Symmetry for Both GGA-PW92 and BLYP DFT Calculations[a]

vibration	NiP[b]	Im GGA	Im BLYP	Im45 GGA	Im45 BLYP	Im(H2O) GGA	Im(H2O) BLYP	N−Me GGA	N−Me BLYP
A_{1g}									
$\nu2$	1574	1563	1540	1562	1547	1564	1542	1559	1538
$\nu3$	1459	1449	1442	1448	1426	1448	1425	1447	1424
$\nu4$	1376	1378	1341	1378	1348	1378	1348	1376	1348
$\nu5$	995	c	c	c	c	1007	c	c	c
$\nu7$	732	727	717	725	711	729	723	723	723
$\nu8$	369	356d	352d	355d	355d	367	355d	353	361d
B_{1g}									
$\nu10$	1650	1632	1598	1632	1595	1633	1599	1629	1596
$\nu11$	1505	1510	1486	1509	1496	1511	1489	1506	1485
$\nu13$	1185	1153	1190	1197	1180	1154	1198	1204	1195
$\nu16$	732	740	725	737	723	743	731	733	731
$\nu18$	237	238	237	239	220	239	239	238	238
A_{2g}									
$\nu19$	1611	1605	1567	1602	1567	1606	1569	1601	1566
$\nu20$	1354	1348	1359	1347	1362	1348	1367	1342	1357
$\nu21$	1317	1332	1303	1329	1299	1332	1312	1327	1309
$\nu22$	1139	1158	1138	1145	1126	1157	1144	1139	1140
$\nu23$	1005	993	c	994	999	1001	c	991	988
$\nu24$	806	804	790	802	c	c	c	799	794
$\nu25$	429	424	432	424	413	431	434	425	429
B_{2g}									
$\nu28$	1505	1488	1465	1485	1456	1490	1467	1483	1462
$\nu29$	1193	1183	1177	1183	1192	1185	1185	1180	1146
$\nu30$	c	1040	1029	c	993	1047	1036	1049	1033
$\nu31$	819	818	817	817	817	818	c	815	818
$\nu35$	197	214	214	216	208	215	219	215	219

vibration	H2O GGA	H2O BLYP	Im GGA	Im BLYP	Im(H2O) GGA	Im(H2O) BLYP	acetate GGA	acetate BLYP	5CO GGA	5CO BLYP
A_{1g}										
$\nu2$	1555	1544	1568	1561	1569	1543	1557	1534	1562	1534
$\nu3$	1439	1424	1448	1442	1449	1421	c	1420	1452	1424
$\nu4$	1370	1348	1375	1367e	1377	1346	1377	1350	1355	1333
$\nu5$	994	c	1025	c	c	c	c	981	987	c
$\nu7$	725	720	731	731	727	724	723	716	711	718
$\nu8$	362d	362d	368	360d	367	351	353d	364d	360	361d
B_{1g}										
$\nu10$	1625	1606	1632	1622	1633	1594	1624	1588	1620	1610
$\nu11$	1501	1489	1512	1501	1513	1486	1498	1478	1515	1485
$\nu13$	1197	1197	1200	1216	1202	1198	1194	1160	1184	1155
$\nu16$	734	732	735	742	735	727	718	711	722	728
$\nu18$	238b	237b	240	241	240	235	233	228	225	238
A_{2g}										
$\nu19$	1592	1572	1607	1595	1607	1565	1595	1556	1577	1575
$\nu20$	c	1366	1342	1371	1345	1366	1335	1335	1337	1346
$\nu21$	1319	1314	1332	1335	1333	1312	1321	1295	1304	1276
$\nu22$	1144	1144	c	c	1141	1146	1141	1292	1125	1107
$\nu23$	c	992	993	1004	986	9991	1000	988	992	995
$\nu24$	794	793	798	c	796	797	799	c	c	789
$\nu25$	434	434	427	428	426	432	421	416	416	429
B_{2g}										
$\nu28$	1477	1469	1489	1484	1489	1466	1481	1459	1476	1463
$\nu29$	c	1183	1174	1191	1173	1156	1177	1180	1165	1184
$\nu30$	1008	1033	1049	1038	c	c	1041	1014	c	1029
$\nu31$	816	818	817	824	817	817	813	813	806	809
$\nu35$	218	217	212	212	213	215	214	215	215	207

[a] Modes classified according to the D_{4h} point group of metalloporphines are listed by irreducible representation. the selected modes are those that are clear in their assignment and not strongly mixed with E_u modes or out-of-plane modes. [b] Data from Li and Spiro.[38] [c] Mixed mode causes identity to be lost. [d] Mixed mode with both in-plane and out-of-plane character. [e] Mixed mode with only in-plane character.

smaller for the same series. For ν_4, $K = 323$ and $A = 6.28$ consistent with only half as large an effect as seen for the core size marker modes (ν_2, ν_3, ν_{10}, and ν_{11}). This is consistent with experimental observations of the smaller dependence of the electron density marker on core size. However, the five coordinate CO adduct (not included in the correlations in Figure 3) shows a modest change in frequency for the core size modes, but ν_4 shifts to 1355 cm^{-1} in excellent agreement with values observed experimentally for five-coordinate heme adducts. There

is almost no effect on in-plane vibrations for the imidazole ligand rotated 45° so that it bisects the Np−Fe−Np angle (IM45) compared to that structure with the imidazole aligned with an Fe−Np bond (IM). The IM and IM45 calculations have identical A_{1g} frequencies and only small 1−2 cm^{-1} shifts in the B_{1g}, A_{2g}, and B_{2g}.

Similar trends in the core size marker modes are found in the BLYP calculation. As mentioned above the core size trend

Table 5. Axial Ligand Vibrational Modes (GGA-PW92/BLYP)

species	acronym	ν_{CO} GGA	ν_{CO} BLYP	δ_{Fe-CO} GGA	δ_{Fe-CO} BLYP	ν_{Fe-CO} GGA	ν_{Fe-CO} BLYP	$\nu_{Fe-N\epsilon}$ GGA	$\nu_{Fe-N\epsilon}$ BLYP	$\delta_{Fe-N\epsilon-Im}$ GGA	$\delta_{Fe-N\epsilon-Im}$ BLYP
Im	IM	2013	1995	578/58	555/560	498	464	283/202, 189/88	270/159,157/86	190/216	188/189
Im	IMA	1977	1952	573/588	559/573	498	462	297/238/ 81	289[a]/237[a]/78a	195/223	171/223
Im(H$_2$O)	IMH2O	2010	1993	570/595	577/587	498	466	279/225[a] /72	273/185/88	203/210	192/205
Im(H$_2$O)	IMAH2 O	1983	1957	573/592	565/568	497	465	297/249[a]/97[a]	280/231/88	186/222	181/218
Im(CH$_3$COHN$_2$)	IMNMA	2013	1988	585/584	552/559	498	464	284/205[a,b]/110[a]	274/209/89	177/191	178/188
Im(CH$_3$CO$_3^-$)	IMACET	1993	1969	594/604	563/573	498	464	298/252[a]/103[a]	280/234/92	202/216	188/196
Im45	IM45	2014	2004	584/588	552/558	495	457	281/196/86	271/181[a]/97	175/184	183/207
H$_2$O	H2O	2012	1994	539/557	531/547	515	490	239	269	128	179
None	5CO	1989	1975	510	505/506	560	534	NA	NA	NA	NA

[a] Significant bending mixed with Fe−Nϵ mode. [b] Split mode. Two modes with close to the same character are found within 5 cm^{-1}.

is maintained here since the $\approx$10−20 cm^{-1} lower frequencies for ν_2, ν_3, ν_{10}, and ν_{11} are consistent with $\approx$0.02 Å larger core size obtained using the BLYP functional. (see Tables 2 and 4). The electron density marker mode also shows about half as large a shift as the remaining core size modes. The calculated effect on core size modes indicates that the level of calculation used is quite reasonable for modeling porphine vibrational spectra. Moreover, the trends indicate that core size expansion is an important contributing factor that will need to be considered further in connection with correlation of axial mode frequencies and the charge relay mechanism.

Axial Vibrational Modes. The axial vibrational modes given in Table 5 consist not only of the observed vibrational modes ν_{Fe-CO} and ν_{CO} but also of axial modes of the imidazole that are not observed in the Raman spectra of six-coordinate hemes. The eigenvectors for these modes are given in the Supporting Information. As will be shown below, these modes are included to account for the apparent lack of a dependence of the ν_{Fe-CO} stretch on the donor strength of the axial ligand (see Table 5). The calculated frequencies given in Table 5 for axial ligand modes that have a contribution from the Fe−Nϵ stretching coordinate include three modes (columns 9 and 10). The highest frequency mode is largely an Fe−C−O doming motion with stationary imidazole (see Supporting Information). This mode has a significant contribution of the Fe−Nϵ internal coordinate to the normal mode. The middle frequency mode has the appearance of an Fe−Nϵ stretch, although some degree of bending is found particularly for anionic imidazole models, and the PED of the Fe−Nϵ internal coordinate is typically the highest for this mode. The lowest frequency mode mostly a collective motion of the Im−Fe−C−O axis with respect to the porphine; however, it too has a small contribution from Fe−Nϵ to the normal mode. The bending modes are also included for completeness. There is a correlation between ν_{CO} in columns 2 and 3 of Table 5 and ν(Fe−Nϵ) in columns 9 and 10 with corresponding to the bond lengths, d(C−O) and d(Fe−Nϵ).[62] [For normal modes it is difficult to define a unique internal coordinate to apply Badger's rule. The correlation used in practice is therefore between the frequency (approximately the square root of the force constant) and the bond length.] For a plot of ν_{CO} vs d(C−O) the correlation coefficients are R(BLYP) = 0.99 and R(GGA) = 0.98. For a plot of ν(Fe−Nϵ) vs d(Fe−Nϵ) one finds R(BLYP) = 0.97 and R(GGA) = 0.67 for a fit to line.

By contrast the ν_{Fe-CO} frequency appears nearly independent of the identity of the axial ligand. As a consequence of this lack of dependence, the calculated frequencies of the Fe−CO stretch and C−O stretch do not follow a simple π-back-bonding correlation. The explanation for the result requires consideration of the trans axial ligands as part of a simple three-body oscillator Im−Fe−CO where the trans imidazole is included in the normal mode. Refinements of models for the axial ligand in five-

coordinate heme adducts have been considered that relax the assumption that the Fe−Nϵ is the sole coordinate involved in PED for axial ligand modes.[63] In the current model calculation the relevant coordinates include both imidazole (Fe−Im) and the porphine−iron axial coordinate (Fe−P). The approximation is three-body treatment of P−Fe−Im, rather than the two-body correlation used in much of the Raman literature that discusses the Fe−Im axial ligand vibration. In the five-coordinate adducts, the refinement is justified on experimental grounds from the need to account for anomalous isotopic shift data. As discussed elsewhere, the isotope shifts are too small to be consistent with the two-body model, but they are consistent with a three-body model in which the Fe−P coordinate is included.[63,64] The reduction in the contribution to the potential energy distribution (PED) from Fe−Nϵ in that case can account for the data. For six-coordinate adducts coupling of Fe−CO and Fe−Im modes across the iron should be considered. Although the PED of the Fe−C coordinate given in Table 6 is rather high for the axial ν_{Fe-CO} mode, there is also a significant and variable contribution from Fe−Nϵ ($\approx$10%). Moreover, Table 7 shows that there is a significant off-diagonal coupling term in the force constant matrix, such that f(Fe−Nϵ)(Fe−C) is $\approx$10−15% of f(Fe−C) and $\approx$25% of f(Fe−Nϵ). These effects can be considered in a simple three-body model, where it can be shown that they are consistent with an absence of shifts for the ν_{Fe-CO} mode. The simple derivation of the three-body equation including coupling (eq 1) is based on the Wilson FG matrix (see Supporting Information). The eigenvalues for the Fe−CO and Fe−Im axial modes are given by

$$\lambda_{\pm} = \frac{((m_1 + m_2)m_3 f_{12} + (m_2 + m_3)m_1 f_{23} \pm \eta^{1/2})}{2m_1 m_2 m_3} \quad (1)$$

$$\eta = (m_1 + m_2)^2 m_3^2 f_{12}^2 + (m_2 + m_3)^2 m_1^2 f_{23}^2 - \\ 2(m_1 m_2 m_3 (m_1 + m_2 + m_3)) \times (f_{12} f_{23} - f_{123}^2) - \\ 2m_1^2 m_3^2 (f_{12} f_{23} - 2f_{123}^2)$$

where m_1 is the mass of the CO, m_2 is the mass of the iron and m_3 is the mass of the imidazole. The force constants are defined as $f_{12} = f$(Fe−CO), $f_{23} = f$(Fe−Nϵ), and $f_{123} = f$(Fe−CO)(Fe−Nϵ). Using the values $m_1 = 28$, $m_2 = 56$, and $m_3 = 68$ au and the values $f_{12} = 1.25$, $f_{23} = 2.72$, and $f_{123} = 0.313$ mdyn/Å from the first row of Table 7 and using the fact that ν(cm^{-1}) = 1303.9$\lambda^{1/2}$, we obtain frequencies of $\nu_{Fe-CO} = 500.4$ cm^{-1} and ν(Fe−Im) = 257.8 cm^{-1}. The agreement with the values from the normal-mode analysis of the entire molecule is quite

(62) Badger, R. M. *J. Chem. Phys.* **1934**, *2*, 128−131.
(63) Franzen, S.; Boxer, S. G.; Dyer, R. B.; Woodruff, W. H. *J. Phys. Chem. B* **2000**, *104*, 10359−10367.
(64) Wells, A. V.; Sage, T. J.; Morikis, D.; Champion, P. M.; Chiu, M. L.; Sligar, S. G. *J. Am. Chem. Soc.* **1991**, *113*, 9655−9660.

Table 6. Potential Energy Distributions Relevant to the Axial Vibrational Modes for (A) the GGA Calculation and (B) the BLYP Calculation

species	ν_{CO}	ν_{Fe-C}	FeCO oop	$\nu_{Fe-N\epsilon}$
		(A) GGA Calculation		
IM	95% C−O	92% Fe−C	7% Fe−Nϵ	36% Fe−Nϵ
	5% Fe−C	6% Fe−Nϵ	2% Fe−C	1% Fe−Np
IMA	95% C−O	88% Fe−C	29% Fe−Nϵ	42% Fe−Nϵ
	5% Fe−C	11% Fe−Nϵ	4% Fe−C	2% Fe−Np
IMH2O	95% C−O	89% Fe−C	19% Fe−Nϵ	30% Fe−Nϵ[a]
	5% Fe−C	8% Fe−Nϵ	5% Fe−C	8% Fe−Np
IMAH2O	95% C−O	87% Fe−C	32% Fe−Nϵ	33% Fe−Nϵ
	5% Fe−C	11% Fe−Nϵ	4% Fe−C	3% Fe−Np
IMNMA	95% C−O	93% Fe−C	6% Fe−Nϵ	57% Fe−Nϵ[a]
	5% Fe−C	6% Fe−Nϵ	2% Fe−C	1% Fe−Np
IMACET	95% C−O	91% Fe−C	21% Fe−Nϵ	9% Fe−Nϵ[a]
	5% Fe−C	9% Fe−Nϵ	3% Fe−C	2% Fe−Np
			10% Nδ−H	44% Nδ−H
		(B) BLYP Calculation		
IM	96% C−O	91% Fe−C	5% Fe−Nϵ	50% Fe−Nϵ
	4% Fe−C	4% Fe−Nϵ	4% Fe−C	36% Fe−Nϵ[a]
IMA	95% C−O	90% Fe−C	12% Fe−N	58% Fe−Nϵ
	5% Fe−C	9% Fe−Nϵ	3% Fe−C	1% Fe−Np
				1% C−Nϵ
				13% Fe−Nϵ−C
IMH2O	96% C−O	93% Fe−C	9% Fe−N	90% Fe−Nϵ
	4% Fe−C	6% Fe−Nϵ	3% Fe−C	
IMAH2O	95% C−O	88% Fe−C	14% Fe−Nϵ	71% Fe−Nϵ
	5% Fe−C	10% Fe−Nϵ	4% Fe−C	4% Fe−C
IMNMA	95% C−O	86% Fe−C	13% Fe−Nϵ	67% Fe−Nϵ[a]
	5% Fe−C	10% Fe−Nϵ	6% Fe−C	1% Fe−Np
				30% Fe−Nϵ−C
IMACET	95% C−O	88% Fe−C	16% Fe−Nϵ	15% Fe−Nϵ
	5% Fe−C	8% Fe−Nϵ	5% Fe−C	5% Fe−C

[a] Multiple low-frequency modes containing Fe−Nϵ character.

reasonable $\nu_{Fe-CO} = 498$ cm^{-1} and $\nu(Fe-Im) = 280$ cm^{-1} as seen in Table 5. The anionic imidazole model IMA can be modeled using the same masses and values of $f_{12} = 1.97$, $f_{23} = 2.67$, and $f_{123} = 0.427$ mdyn/Å from the second row of Table 5. Note that the force constant for Fe−C stretching has decreased commensurate with the longer bond length. However, the frequency for the ν_{Fe-CO} stretch calculated from eq 1 is 499.7 cm^{-1}, a shift of only 0.7 cm^{-1}. This shift would not even be noticed if we rounded off to three significant figures as we have done for the calculated frequencies from the GGA and BLYP functionals in Tables 4 and 5. Equation 1 predicts that $\nu(Fe-Im)$ increases to 320.1 cm^{-1}, which is larger than the increase observed in the modes that depend on Fe−Nϵ, but is in the correct direction. Of course, the PEDs are redistributed and mixing with bending coordinates is important in the all-atom calculation. These effects are ignored in eq 1. The point of this discussion is that an increase in $f(Fe-N\epsilon)$ from 1.25 to 1.97 has an affect on the ν_{Fe-CO} frequency that offsets the expected decrease by about 2 cm^{-1}, and the increase in the $f(Fe-N\epsilon)$-(Fe−C) offsets the decrease by about 3 cm^{-1} leading to an essentially equal value despite the large change in axial ligation in the IM and IMA molecules. These effects are further evident in a comparison of the PED for the ν_{Fe-CO} mode in Table 6. The PED of $f(Fe-C)$ decreases from 92% for IM to 88% for IMA and there is a corresponding increase in the contribution of $f(Fe-N\epsilon)$ consistent with this explanation. The three-body approach works well for the IMH2O and IMAH2O calculations as well, but does not work for the IMNMA and IMACET calculation. The three-body model is useful because it helps to rationalize a complicated description that arises from the total normal coordinate analysis including 48 masses (for the IM molecule) in terms of a few parameters. It clearly does not account for all of the factors, but it can explain how it is that

both GGA and BLYP calculations indicate an essentially constant value ν_{Fe-CO} throughout the series of molecules studied here.

It is important to relate the calculations presented here to the experimental π-back-bonding relationship obtained for imidazole containing heme proteins, specifically globins and peroxidases. The present calculation appears to explain ν_{CO} frequency lowering in quantitative terms. It also suggests that ν_{Fe-CO} does not depend strongly on axial ligation. There are two points that are worth noting in this context. First, the model does not consider equatorial effects or distal trans effects. Equatorial effects that may influence π-back-bonding include changes in the protein electrostatic environment among different proteins. These have been modeled by studying the inductive effect of substituted porphines, and the π-back-bonding correlation is observed for a series of molecules where fluoro-, chloro-, or amino-substituted porphines have been compared.[43] Distal effects have been studied by semiempirical methods using a unit charge at fixed distances from the CO ligand.[11] In that case, as well, a π-back-bonding correlation was found. Using the methods presented here (both GGA and BLYP) π-back-bonding correlations are found in calculations where systematic changes in axial charge density do not significantly affect the core size of the heme (Franzen, manuscript in preparation). Thus, a major difference between this study and preceding studies is the effects found that involve coupling of axial ligand to the heme core size. A second point that needs to be addressed is the calculational method used. It is possible that post-Hartree−Fock calculations with extensive configuration interaction would reveal a different picture than that obtained by DFT. For example, a comparison of a simple model for Im−Fe−CO with four amidinato groups instead of a porphine molecule was carried out using both MP2 and BLYP calculations for both a neutral and anionic imidazole (analogous to IM and IMA with four NH$_2^{\delta-}$ groups instead of porphine). The Fe−Np, Fe−Nϵ, Fe−C, and C−O distances are given in Table 8. Both the MP2 and BLYP calculations agree that both the Fe−C and C−O bonds increase as the ligand becomes more basic. This trend is the same as that found for the GGA and BLYP porphine models studied here (Figure 1 and Table 2). While the agreement in terms of structure is encouraging, it does not prove that CI has been adequately treated. It has been suggested that CI is necessary to correctly determine the energy level of the Nϵ lone pair in heme enzyme model calculations.[65,66] However, the excellent agreement of the in-plane vibrational modes (Figure 3) and correct relationship of ν_{CO} with experimental trends (Tables 3, 5, and 12) are a good indication that the DFT approach provides reasonable treatment of the ground-state vibrational modes of interest. The result obtained here is reasonable when one considers the fact that axial ligation has a substantial σ-bonding character and that experimental trends for different axial ligands such as thiolates in cytochromes P-450 show a *parallel* frequency lowering for both ν_{Fe-CO} and ν_{CO}.[1,26] [This effect may be responsible for the fact that a number of ν_{Fe-CO} bands observed in the Raman spectrum of peroxidases and that there is not always a strong correlation between the ν_{Fe-CO} and ν_{CO} bands when multiple bands are present.]) Such a parallel frequency lowering is implied by the correlation of $d(Fe-C)$ and $d(C-O)$ in Table 2. The conclusion of this work is that the expected frequency lowering is largely offset by compensating σ-bonding and π-bonding effects as seen in the tradeoff between the core size effects and axial ligand effects.

(65) Stavrov, S. S.; Decusar, I. P.; Bersuker, I. B. *Mol. Biol. (translated from Russian)* **1988**, *22*, 677−682 (Part 2).

(66) Bersuker, I. B.; Stavrov, S. S. *Coord. Chem. Rev.* **1988**, *88*, 1−68.

Table 7. Force Constants and Interaction Force Terms for the Stretching Internal Coordinates Relevant to the Axial Vibrational Modes Obtained from (A) the GGA Calculation and (B) the BLYP Calculation

species	f(Fe$-$Nϵ)	f(Fe$-$Np)	f(C$-$O)	f(Fe$-$C)	f(C$-$O)(Fe$-$C)	f(Fe$-$Nϵ)(Fe$-$C)	f(Fe$-$Nϵ)(C$-$O)
				(A) GGA Calculation			
IM	1.25	1.57	16.6	2.7	1.00	0.313	0.075
IMA	1.97	1.55/1.42	16.1	2.67	1.01	0.427	0.118
IMH2O	1.43	1.56/1.45	16.	2.71	1.01	0.33	0.078
IMAH2O	2.00	1.56/1.43	16.	2.64	1.01	0.414	0.124
IMNMA	1.29	1.56	16.6	2.7	1.03	0.339	0.077
IMACET	1.60	1.44/1.4	16.2	2.77	0.98	0.381	0.140
				(B) BLYP Calculation			
IM	0.85	1.48	16.5	2.33	1.03	0.241	0.081
IMA	1.44	1.35	15.8	2.33	1.00	0.25	0.119
IMH2O	1.01	1.50	16.5	2.39	1.0	0.24	0.085
IMAH2O	1.5	1.3	15.9	2.30	1.00	0.215	0.122
IMNMA	1.37	1.5	16.	2.25	1.04	0.215	0.083
IMACET	1.21	1.4	16.1	2.3	1.01	0.283	0.139

Table 8. Geometries of the M1 Model Obtained from BLYP, MP2, and Hartree$-$Fock Calculations

species	Fe$-$Np	Fe$-$Nϵ	Fe$-$C	C$-$O
BLYP M1 IMA	1.942	2.072	1.821	1.191
BLYP M1 I	1.920	2.133	1.794	1.183
MP2 M1 IMA	1.900	2.064	1.868	1.187
MP2 M1 IM	1.911	2.169	1.824	1.183
HF M1 IMA	1.849	1.952	3.397	1.135
HF M1 IM	1.853	2.066	2.072	1.128

Table 9. Mulliken Charges for Serine Protease Catalytic Triad Model

ligand	Nδ	Nϵ	O
IM	-0.273	-0.424	-0.519
IMH2O	-0.279	-0.430	-0.514
IMNMA	-0.279	-0.438	-0.520
IMACET	-0.300	-0.473	-0.558
IMA	-0.410	-0.500	-0.570
IMAH2O	-0.488	-0.491	-0.565

Table 10. Mulliken Charges for Ferrous Oxy Porphine

ligand	Nδ	Nϵ	Np	Fe	O	O
IM	-0.252	-0.355	-0.529	0.999	-0.121	-0.114
IMH2O	-0.281	-0.367	-0.529	1.003	-0.131	-0.185
IMNMA	-0.350	-0.368	-0.526	1.031	-0.131	-0.178
IMACET	-0.389	-0.390	-0.515	0.998	-0.144	-0.162
IM	-0.415	-0.419	-0.505	1.030	-0.171	-0.247
IMAH2O	-0.431	-0.408	-0.509	1.026	-0.156	-0.231

is very similar for both the GGA-PW92 and BLYP functionals. It can be represented as N$\delta^{\delta-}-$N$\epsilon^{\delta-}-$Np$^{\delta+}-$Fe$^{\delta+}-$C$^{\delta-}-$O$^{\delta-}$. Choosing the comparison between IMA and IM as representative, the increased negative charge of ≈-0.2 on Nδ is due to abstraction or polarization of the Nδ hydrogen. The effect on Nϵ is also an increase in negative charge density of ≈-0.05, which is almost exactly the same increase in negative charge density on the terminal oxygen of bound CO. Charge density moves from the iron $\approx+0.02$ and pyrrole nitrogens $\approx+0.02$ to the carbon of CO ≈-0.03. Although the comparison between IM and IMA was used here, Table 12 shows that there is an excellent correlation for the Mulliken charge parameters for all six test molecules studied here according to both the GGA and BLYP methods. Table 12 also shows that the frequency of ν_{CO} is proportional to the negative charge on the terminal oxygen of CO. This strong correlation indicates that ν_{CO} is an important experimental marker for the charge relay.

Comparison of species that have reduced trans ligand strength such as H2O or 5CO also have lower ν_{CO} frequencies (ν_{CO}(5CO) < ν_{CO}(H2O) < ν_{CO}(IM) < ν_{CO}(IMH2O)). This frequency-lowering effect arises from the decrease in the Fe$-$C bond length leading to stronger π-back-bonding without an associated charge relay effect. As the axial ligation gets weaker the intrinsic iron interaction with the CO dominates and although the charge distribution on CO changes little the C$-$O bond is weakened at the expense of a strengthened Fe$-$CO bond in a classic π-back-bonding interaction. The extreme limit of this is the five-coordinate CO adduct (5CO), which shows a large increase in ν_{Fe-CO} and a decrease in ν_{CO}. The lowering of ν_{CO} due to weakened axial ligation and a shorter C$-$O bond length can be contrasted with the effect increasing the negative charge on proximal imidazole, because for the series 5CO, H2O, IM, IMH2O there is essentially no change in the charge of the terminal oxygen.

Effects of the Charge Relay on the σ-Bonding and π-Bonding Molecular Orbitals. The essence of the charge relay consists of a simultaneous decrease in σ-bonding and increased π-back-bonding of bound CO resulting from increased Nϵ charge density, which in turn arises from an increase in the

Thus, equatorial and distal effects may be the principal explanation for the observed π-back-bonding correlation. Given the wealth of mutants available in the peroxidase and globin protein families it should be possible to use DFT methods to determine the relative extent of distal, proximal and equatorial contributions to the observed experimental correlation between ν_{Fe-CO} and ν_{CO}.

Electrostatic Correlations. In the catalytic triad of serine proteases, the effect of the charge relay is an increase in the nucleophilicity of the serine $-$OH group (shown as methanol in the model system) in Figure 2. The increase in the negative Mulliken charge on the serine oxygen can be seen in Table 9. Note that the negative charge on O increases proportionally to the charge on Nϵ. The charges follow a trend consistent with a dominant contribution from σ-bonding by Nϵ that is further corroborated by the hydrogen bonding potential energy surfaces presented below.

The charge relay mechanism results in an increase in electron density on the terminal oxygen of iron-bound oxy or peroxide. The charge distributions calculated in Tables 10 and 11 using Mulliken charges support these expected trends in the iron$-$porphine$-$O$_2$ and iron$-$porphine$-$CO models. The magnitude of the charge on the terminal oxygen for the carbonmonoxy adduct found for both the GGA-PW92 and BLYP functionals follows the degree of polarization of the imidazole due to hydrogen bonding at the Nδ proton of the imidazole (IMA > IMAH2O > ACETIC > NMACET > IMH2O > IM $\approx$ IM45). The charge relay indicated by the pattern of Mulliken charges

Table 11. Mulliken Charges for Ferrous Carbonmonoxy Porphine

| ligand	$N\delta$ GGA	$N\delta$ BLYP	$N\epsilon$ GGA	$N\epsilon$ BLYP	Np GGA	Np BLYP	Fe GGA	Fe BLYP	C GGA	C BLYP	O GGA	O BLYP
IM	−0.254	−0.249	−0.330	−0.342	−0.518	−0.538	0.827	0.606	0.190	0.305	−0.239	−0.250
IMA	−0.429	−0.449	−0.385	−0.391	−0.494	−0.516	0.842	0.614	0.157	0.271	−0.283	−0.292
IMH2O	−0.281	−0.273	−0.336	−0.346	−0.516	−0.537	0.829	0.606	0.188	0.303	−0.242	−0.252
IMAH2O	−0.439	−0.456	−0.378	−0.384	−0.497	−0.520	0.841	0.613	0.162	0.277	−0.278	−0.288
IMNMA	−0.271	−0.265	−0.338	−0.345	−0.513	−0.534	0.827	0.605	0.185	0.296	−0.243	−0.254
IMACET	−0.334	−0.308	−0.371	−0.370	−0.504	−0.524	0.841	0.609	0.171	0.286	−0.270	−0.280
IM45	−0.253	−0.249	−0.329	−0.337	−0.516	−0.536	0.829	0.603	0.18	0.303	−0.238	−0.249
H2O	NA	NA	−0.438[a]	−0.403	−0.489	−0.552	0.554	0.620	0.284	0.301	−0.18	−0.247
5CO	NA	NA	NA	NA	−0.547	−0.547	0.563	0.588	0.291	0.295	−0.182	−0.251

[a] Charge on oxygen of proximal H_2O ligand.

Table 12. Correlations of the Mulliken Charges

charge correlation	GGA intercept, slope (R)	BLYP intercept, slope (R)
$N\epsilon$ vs $N\delta$	−0.26, 0.28 (0.94)	−0.29, 0.22 (0.95)
O vs $N\epsilon$	0.034, 0.82 (1.00)	0.055, 0.89 (0.99)
C vs $N\epsilon$	0.38, 0.58 (0.99)	0.52, 0.63 (0.98)
Np vs $N\epsilon$	−0.65, −0.41 (0.99)	−0.69, −0.43 (0.99)
Fe vs $N\epsilon$	0.73, −0.30 (0.98)	0.55, −0.18 (0.98)
ν_{CO} vs O	2221, 845 (0.95)	2236, 965 (0.99)

$N\delta$−H charge due to hydrogen bonding or hydrogen abstraction. A model calculation on imidazole indicates that the $N\epsilon$ lone pair is significantly raised in energy as the $N\delta$−H is abstracted, while the π-bonding MOs of imidazole are less affected (see Supporting Information). Thus, it is not principally the π-electron density on the imidazole that affects π-bonding on the trans CO ligand. Rather it is the expansion of the core size that affects π-bonding. The consistency of this model of the bonding is considered in the following.

The Fe−$N\epsilon$ and Fe−C bond lengths are inversely correlated indicating that increased charge density on $N\epsilon$ causes a repulsion of the trans CO ligand. The Fe−CO repulsion arises from increased electron density in an antibonding orbital that involves the $N\epsilon$ lone pair, CO lone pair, and Fe d_{z^2}. This picture would seem to indicate that σ-antibonding effects dominate. However, this preliminary conclusion must be reconciled with the fact that both the Fe−C and C−O bond lengths are found to increase in the series IMA > IMAH2O > IMACET > IMNMA > IMH2O > IM, i.e., as the basicity of the trans ligand is increased. There is no such thing as a simple axial σ-bonding effect in a metalloporphyrin since an increase in the Fe−C bond length necessarily results in a decrease in the π-overlap with the iron and a concomitant decrease in π-back-bonding. Thus, the C−O bond should shorten as the Fe−C bond lengthens. However, both the experimental π-back-bonding correlation and the calculated C−O bond length indicate that π-back-bonding actually *increases* as the trans axial ligand σ-donor strength increases. The axial and equatorial π-bonding effects that arise from the shortened Fe−Np bond length account for the calculated and experimental trends.

The core size marker shifts shown in Figure 3 and the Fe−Np bond lengths are consistent with a decrease in equatorial π-bonding as the trans-axial donor strength increases. This means that more iron $d\pi$ electron density and even perhaps some imidazole π-electron density is available for overlap with the CO π^* orbitals. The decrease in overlap of iron $d\pi$ orbitals with the ring increases electron density available for the CO. This can be seen in the trends found in the Mulliken charges given in Table 11. As the electron density decreases on the pyrrole nitrogens and the iron, it increases on the carbonyl carbon and oxygen. The result of the increase in π-bonding density on CO will be to offset the weakening of the Fe−C bond due to
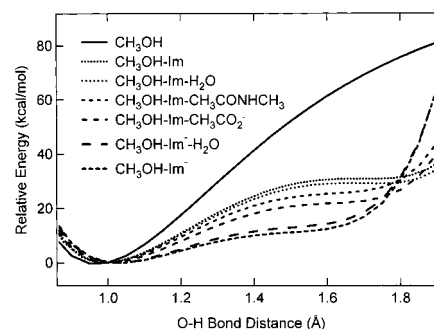
Figure 4. Calculated hydrogen bond potential energy surfaces for the hydrogen atom transfer reaction CH_3O−H⋯Im → CH_3O^-⋯H−Im.

σ-antibonding interactions with trans imidazole. In addition, the C−O bond will be lengthened and its vibrational force constant lowered. Thus, the porphine ring is an essential mediator of the π-back-bonding effect and serves to permit a simultaneous weakening of both Fe−C and C−O bonds. The π-bonding effect more than compensates for the σ-antibonding effect on the Fe−C bond, and this bond actually increases in parallel with the C−O bond length as seen in Tables 2 and 3. These predicted trends agree with calculated bond length and frequency trends and with the experimental trends in the C−O stretching frequency.

Potential Energy Surfaces for the Effect of Hydrogen Bonding of Imidazole in a Charge Relay Mechanism. The Asp-His-Ser catalytic triad of serine proteases shown in Figure 2 has been studied in terms of the hydrogen bond between the serine oxygen (methanol in the model) and histidine $N\epsilon$ (imidazole in the model). In Figure 4, the potential energy surface for hydrogen along a CH_3O−H⋯Im → CH_3O^-⋯H−Im coordinate in the catalytic triad is plotted as a function of the distance from the oxygen nucleus. Stronger hydrogen bonding to $N\delta\angle H$ leads to greater basicity of $N\epsilon$ as indicated by the trend in the Mulliken charge in Table 9. The negative charge on the imidazolate of the IMA model shows the greatest change in electron density of $N\epsilon$ as well as the greatest stabilization of the hydrogen atom in the $N\epsilon$⋯H−O hydrogen bond (≈ 51 kcal/mol relative to methanol). Significant stabilization is achieved by acetate (≈ 43 kcal/mol relative to methanol) and even H_2O hydrogen-bonded to $N\delta$−H has a profound effect (≈ 31 kcal/mol relative to methanol). The relative energies of the various hydrogen bonded species tracks the negative Mulliken charge on the serine oxygen; i.e., larger negative charge density is correlated with lower energy of deprotonation. The comparison of the serine protease catalytic triad with peroxidase models serves to underscore the fact that σ-bonding contributions from the imidazole are important in both. Furthermore, as we have seen above, π-bonding effects must be considered in the peroxidase model, while these do not appear to play a major role in the serine protease catalytic triad.
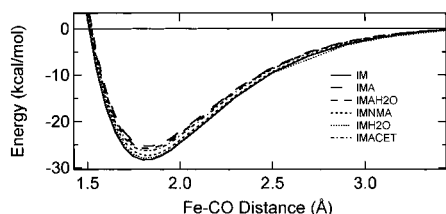
Figure 5. Potential energy surface for the Fe–CO bonding interaction. The surfaces have been calculated for each of the six hydrogen bond partners described in Table 1.
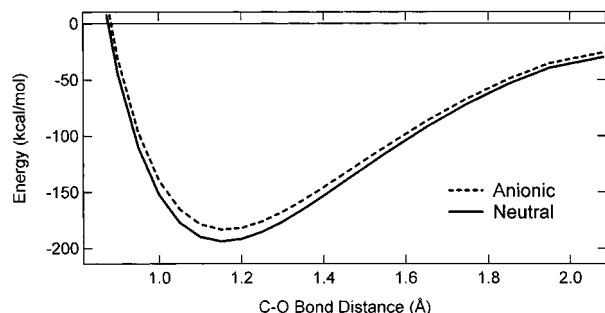

Figure 6. Potential energy surface for the C–O bond. The surfaces fall into two groups, anionic (dashed line) and neutral (solid line). The potential energy surfaces for IM and IMA are given as representative for each of the groups.

The potential energy surfaces for both Fe–CO and C–O bond dissociation have been studied for the iron–porphine–CO model molecules shown in Figure 1. Figure 5 shows the potential energy surface for the Fe–CO coordinate. The ordering of the effect on binding is the same as for the Asp-His-Ser model above. The trend indicates that increased basicity trans to the CO ligand weakens the Fe–CO bond, but the effect is significantly smaller than for the deprotonation of the serine hydroxyl shown in Figure 4. The negatively charged model adducts IMA, IMAH2O, and IMACET weaken the trans Fe–CO bond to the greatest extent ($\approx$3 kcal/mol). The hydrogen bonding ligands show small effects on trans CO bonding (e.g. $\approx$0.4 kcal/mol for IMH2O).

The ν_{CO} frequencies and bond lengths are indicative of a weakening of the C–O bond as the trans axial ligand basicity increases. The weakened C–O bond is also manifest in the potential energy surface shown in Figure 6. The neutral hydrogen bond partners have essentially no effect and are identical to the IM potential energy surface (the solid line in Figure 6). The negatively charged hydrogen bond partners (IMA, IMAH2O, IMACET) weaken the C–O bond by $\approx$9.5 kcal/mol and are nearly identical to the IMA potential energy surface (shown as the dashed line in Figure 6). The weakening of the bond for the IMA, IMAH2O, and IMACET molecules is consistent with their longer C–O bond lengths compared to the neutral imidazole models. The average of $\approx$1.162 Å for $d(C–O)$ for IMA, IMAH2O, and IMACET should be compared to an average of $\approx$1.157 Å for IM, IMH2O, and IMNMA. This longer bond is associated with greater polarization as seen for the Mulliken charges for terminal oxygen, which are substantially larger for the anionic than for the neutral hydrogen bonded species. Importantly these factors are correlated with the ν_{CO} frequency as well. The average ν_{CO} frequency for the neutral species is 2012 cm^{-1} and that for anionic species is 1984 cm^{-1} for the GGA calculation. The calculations indicate that vibrational frequencies have relevance for interpretation of proximal charge effects in peroxidases. The bond lengthening that is calculated here is correlated with an increased negative charge density on the terminal oxygen and a decrease in the bonding energy of the C–O bond. The calculated frequency in turn follows similar trends and agrees with experimental observations of lower ν_{CO} stretching frequencies in peroxidases than in globins.

Conclusion

The effect of axial ligand charge relay on the $\nu_{Fe–CO}$ and ν_{CO} frequencies has been studied in order to correlate observed frequencies with electronic structure. The DFT calculations indicate that there is a substantial σ-bonding effect as hydrogen bonding to the Nδ–H proton increases the negative charge density on the imidazole ring. However, unlike models of serine proteases where the Nϵ charge density also becomes significantly more negative, the charge is transmitted to the trans axial ligand with concomitant effects on the porphine ring due to core size expansion. As the Nϵ donor strength increases the Fe–Nϵ bond shortens and the porphine ring expands reducing π-overlap of the ring with the dπ orbitals of the iron. The increased Fe–Np distance converts axial changes in σ-bonding into π-bonding effects. The charge density on the iron is delocalized into the π^* orbital of bound CO. Thus, the core size expansion permits increased π-back-bonding rather than decreased π-back-bonding that would be expected for a lengthening of the Fe–C bond alone. The effect is seen in the simultaneous lengthening of the Fe–C and C–O bonds. This is reflected in vibrational spectra that show a decrease ν_{CO} stretching frequency as the trans axial ligand strength increases and as the Fe–Nϵ bond shortens. However, the calculations do not show the frequency lowering expected for a longer Fe–C bond. Nor do they show a classical inverse proportionality expected for π-back-bonding. In fact, the $\nu_{Fe–CO}$ stretch is nearly constant through the series of molecules studied by two DFT functionals. The competing factors that lead to a lack of change in the Fe–CO frequency include an increased force constant of the trans imidazole and stronger coupling as the two force constants become more similar. The Fe–C bond is lengthened by a σ-antibonding interaction and simultaneously stabilized by a stronger π-donor interaction from the iron arising from core size expansion of the porphine ring, and perhaps increased π-bonding of the trans imidazole as well. One explanation for disagreement with experimental back-bonding correlations is that the π-back-bonding correlation may arise from distal effects. Further studies will address this point both by considering distal hydrogen bonding and by systematic comparison of the structures considered here as a function of constrained bond length to reveal trends that are difficult to ascertain when comparing different molecules. In general, the approach taken here has been to obtain general trends for six molecular models that represent possible hydrogen bonding scenarios of biological relevance.

The functional consequence of the charge relay can be described as follows. Increased hydrogen bonding on Nδ–H causes a redistribution of electron density on imidazole such that there is a significant increase in donor character of the imidazole π-system as well as the expected effect on the Nϵ lone pair. The effect of increased σ-bonding by the Nϵ lone pair weakens the trans Fe–C bond. Without any compensating effects the weakened Fe–CO interaction would lead to a higher C–O stretching frequency because of a reduction in the π-back-bonding. However, increased π-bonding from the porphine ring polarizes the Fe–C–O moiety further while simultaneously weakening the C–O bond. A similar effect is calculated in Fe–O–O models indicating that the terminal negative charge of

bound diatomic oxygen would also increase under the same conditions. The observed effect of the charge relay corresponds with an intuitive picture of the effect of increasing electron density of the imidazole ligand to iron supporting higher oxidation states of the iron as needed for peroxidase function. The net effect of the combined σ- and π-bonding interactions is a weakening of the O$-$O bond and a polarization of the terminal oxygen commensurate with the requirements for O$-$O bond scission in the peroxidase mechanism. The model calculations demonstrate that the ν_{CO} stretching frequency is an excellent probe of the trans axial effects. Further work should also include comparisons with oxy and peroxy species will help to determine the connection of these observables with specific energetic barriers in the mechanism. Once this is done, quantitative comparison of the ν_{CO} stretching frequency with charge density will lead to a means of systematically characterizing charge density in peroxidases.

Supporting Information Available: Tables listing energy levels and molecular orbitals from the GGA calculation, figures showing comparisons of the energy levels for different model calculations, the imidazole calculation including MO representations, an energy diagram as a function of Nd$-$H distance, the eigenvectors for the axial ligand modes, and the molecule derived from model M1, and text describing the derivation of eq 1 and the model M1 (PDF). This material is available free of charge via the Internet at http://pubs.acs.org.

JA0108988